142 (2025) 205683

Contents lists available at ScienceDirect

Gas Science and Engineering

journal homepage: www.journals.elsevier.com/gas-science-and-engineering

Techno-economic assessment of pressure swing adsorption tail gas decarbonisation for blue hydrogen production

Ayub Golmakani [a], Navid Khallaghi [a,e,*], Amirpiran Amiri [b], Vasilije Manovic [c,d], Seyed Ali Nabavi [a,e]

[a] Centre for Climate and Environmental Protection, Cranfield University, Bedfordshire, Bedford, MK43 0AL, UK
[b] School of Engineering and Applied Science, Aston University, Birmingham, B4 7ET, UK
[c] Chemical Engineering Department, King Fahd University of Petroleum & Minerals, Dhahran, 31261, Saudi Arabia
[d] Interdisciplinary Research Center for Hydrogen Technologies and Carbon Management, King Fahd University of Petroleum & Minerals, Dhahran, 31261, Saudi Arabia
[e] Centre for Energy Decarbonisation and Recovery (CEDAR), Cranfield Univeristy, Bedforshire, Bedford, MK43 0AL, UK

ARTICLE INFO

Keywords:
Blue hydrogen
PSA tail gas
SOFC
CLC
Oxy-combustion

ABSTRACT

Steam methane reforming (SMR) is a leading technology for hydrogen production. However, this technology is still carbon-intensive since, in current SMR units, the PSA tail gas containing H_2, CO, and CH_4 is burned at the reformer with air and exits the stack at a CO_2 purity of less than 5 %, which is not feasible to capture. In this paper, we aim to either harness the energy content of this gas to generate power in a solid oxide fuel cell (SOFC) or burn it via chemical looping combustion (CLC) or oxy-combustion process to produce off-gas with high CO_2 purity ready to storage. Therefore, an industrial-scale PSA with 72,000 Nm^3/h feed capacity was modelled to obtain the tail gas flow rate and composition. Then, CLC, SOFC, and oxy-combustion were modelled to use tail gas. Finally, a techno-economic analysis was conducted to calculate each technology's levelised cost of hydrogen (LCOH). It was observed that CO_2 purity for CLC meets the criteria for storage (>95 %) without further purification. On the other hand, from the economic point of view, all three technologies show a promising performance with an LCOH of 1.9 €/kg.

1. Introduction

Clean hydrogen is known as an alternative to fossil fuels to reduce greenhouse gas emissions. Various hydrogen production methods are: (1) biomass or coal gasification (Ahn et al., 2012; Higman, 2008; Seyitoglu et al., 2017), (2) partial oxidation of heavy hydrocarbons (Reed and Kuhre, 1980; Steinberg and Cheng, 1989), (3) ammonia reforming (CHO et al., 1998; Yáñez et al., 2020), (4) pyrolysis (Barbarias et al., 2018; Duman and Yanik, 2017; Schneider et al., 2020), (5) auto-thermal reforming (ATR) (Zhou et al., 2020), (6) thermochemical water splitting (Mehrpooya and Habibi, 2020), and (7) water electrolysis with renewable energy (solar, wind, …) or nuclear energy (Pinsky et al., 2020). However, the mentioned technologies suffer from a low technology readiness level (TRL) except for commercially available reforming and water electrolysis.

Hydrogen production via steam methane reforming (SMR) and pressure swing adsorption (PSA) downstream for further purification is the most promising technology pathway in the near term to meet the net-zero targets by 2050 (Golmakani et al., 2022). However, this technology is still carbon-intensive. The PSA tail gas (containing combustible gases such as H_2, CH_4, and CO, along with a significant amount of CO_2) is burnt with air at the reformer, leading to a low CO_2 purity (less than 5 %), which makes the decarbonisation cost-intensive. Hence, finding an affordable PSA tail gas decarbonisation solution is necessary.

Pellegrini et al. (2020) investigated an aqueous methyldiethanolamine (MDEA) solution to capture 96 % of the CO_2 in the tail gas of a PSA unit producing 100,000 Nm^3/h of hydrogen. They concluded that amine-based technologies are energy-intensive for CO_2 capture from PSA tail gas. Baojun et al. (Li et al., 2016) used the membrane process to treat the PSA tail gas in a PSA-membrane hybrid process that produced hydrogen with 99.98 % purity at a 91.71 % recovery. Golmakani et al. (2016) studied a pressure vacuum swing adsorption (PVSA) process, and they screened different adsorbents, including activated carbon, zeolite 5A, and SAPO 34, to capture CO_2 from tail gas. However, PVSA was still suffering from energy intensity since there was a compressor at the feed to increase tail gas pressure from atmospheric to adsorption pressure

* Corresponding author.
E-mail address: n.khallaghi@cranfield.ac.uk (N. Khallaghi).

https://doi.org/10.1016/j.jgsce.2025.205683
Received 22 December 2024; Received in revised form 22 May 2025; Accepted 1 June 2025
Available online 10 June 2025

and a vacuum pump to regenerate the adsorbents at below atmospheric levels.

Despite extensive research on PSA tail gas treatment for hydrogen production, existing decarbonisation methods such as amine-based absorption, membrane separation, and pressure swing adsorption remain energy-intensive, and economically and environmentally challenging. Hence, this work explores oxy-combustion and chemical looping combustion (CLC) as alternative PSA tail gas utilisation strategies, which have not been adequately studied in this context. Hence, this research aims to assess the technical and economic feasibility of three alternative PSA tail gas utilisation: oxy-combustion, CLC, and solid oxide fuel cell (SOFC), to determine their potential for enhancing CO_2 capture and reducing the overall cost of blue hydrogen production from steam methane reforming. Unlike conventional approaches, oxy-combustion eliminates nitrogen dilution without requiring high-pressure compression (Khallaghi et al., 2020), while CLC provides in-situ oxygen transfer without needing an energy-intensive air separation unit (ASU) (Khallaghi et al., 2019a). Additionally, this study integrates SOFC to evaluate the potential for direct power generation from PSA tail gas. By developing a detailed process model using Aspen Adsorption (Adsim) and Aspen Plus v12.1, followed by a techno-economic analysis, this work provides a comparative assessment of these novel pathways in terms of hydrogen production efficiency and cost-effectiveness, offering valuable insights into low-carbon hydrogen production strategies.

2. Process description and model development

SMR units' syngas passes through water gas shift (WGS) reactors to increase hydrogen yield and convert CO to CO_2. The effluent gas of the WGS process, which is enriched with H_2 (stream 1), is further purified at a PSA unit to produce ultra-pure hydrogen (>99.9 %, stream 2). However, the PSA tail gas (stream 3) contains flammable gases such as H_2, CH_4, and CO and is burned with air at existing SMR units, leading to a low CO_2 purity (CO_2<5 %) gas at the stack that is costly to capture CO_2. Fig. 1 This schematic depicts three processes for utilising PSA tail gas (stream 3). The first is a CLC process that provides the O_2 for tail gas combustion from a metal oxide rather than air with a high amount of N_2, which lowers the CO_2 purity. Therefore, after condensation, the effluent gas from the burner stack contains high CO_2 purity (stream 4). Fig. 1b shows SOFC integration for electricity and heat production. The exhaust gas of the SOFC burns at the afterburner with pure oxygen, and water is separated in a condenser (stream 5). Finally, Fig. 1c illustrates the implementation of high-purity oxygen to combust the tail gas, resulting in high-purity CO_2 in the exhaust gas with N_2 elimination (stream 6).

2.1. PSA process

The PSA process comprises 9 beds with 18 steps and three equalisation steps to maximise the hydrogen recovery, Table 1. A two-layered bed of activated carbon and zeolite 5A were used as adsorbents inside each bed. The type of selected adsorbents affects the PSA performance. Golmakani et al. (2016) and Tamnanloo et al. (Tamnanloo et al., n.d.) have conducted some studies on the impact of adsorbents. This paper selected two commercially available adsorbents used in most current industries. The input flow rate of the PSA process and operating conditions are mentioned in Table 2. This configuration enables three beds to adsorb impurities at each moment; therefore, high hydrogen recovery and productivity are achievable. In addition, the effluent gas of each bed after the third equalisation depressurisation (ED3) provides a purge (PPG) for the regeneration of the bed in the purge step (PG).

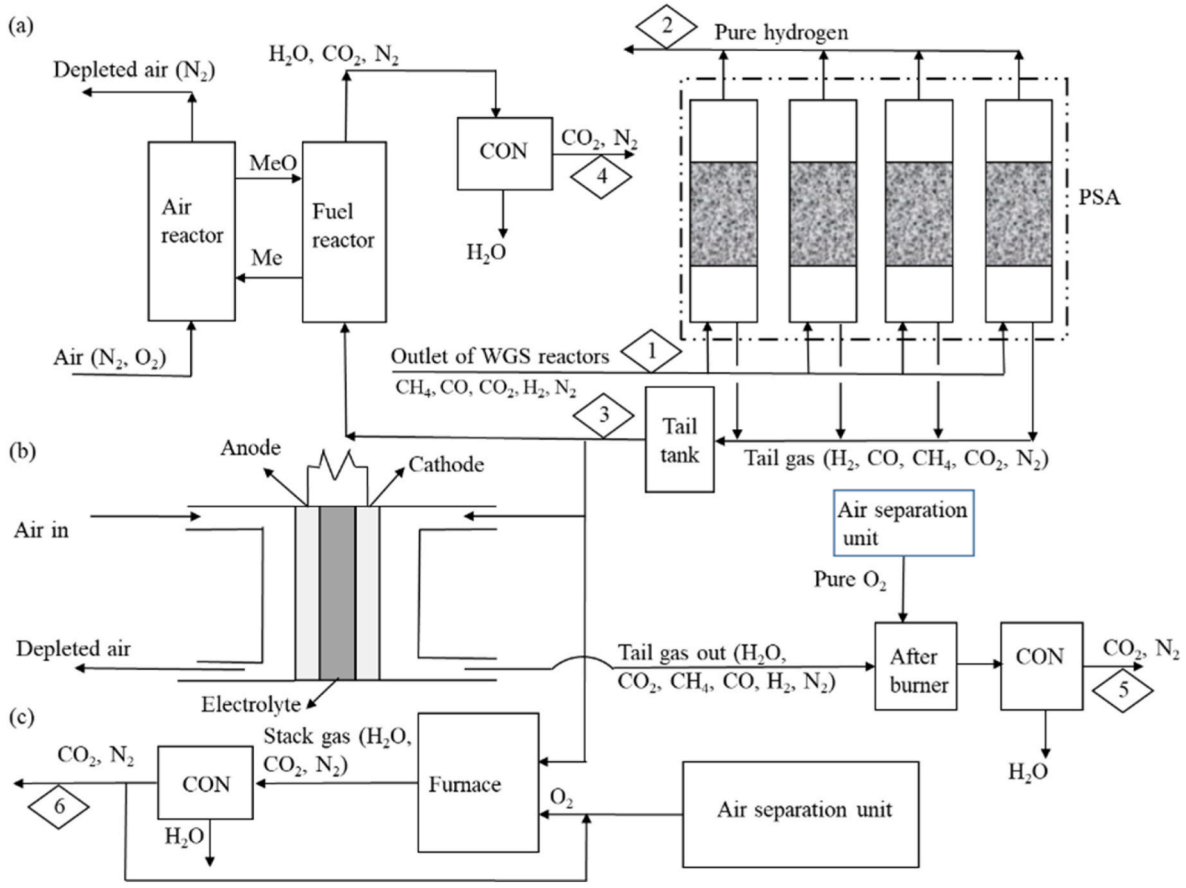

Fig. 1. Schematic of three different PSA tail gas utilisation processes. (a) chemical looping combustion (CLC), (b) solid oxide fuel cell (SOFC), and (c) oxy-combustion. Legend: CON: condensation, PSA: pressure swing adsorption, WGS: water gas shift.

Table 1
The steps of a 9-bed PSA process for hydrogen purification.

9-BED PSA Steps																		
Steps		A						B						C					
		A1	A2	A3	A4	A5	A6	B1	B2	B3	B4	B5	B6	C1	C2	C3	C4	C5	C6
BED	1	AD						ED1	ED2	ED3	PPG		BD	PG		EP1	EP2	EP3	RP
	2	EP3	RP	AD						ED1	ED2	ED3	PPG		BD	PG		EP1	EP2
	3	EP1	EP2	EP3	RP	AD						ED1	ED2	ED3	PPG		BD	PG	
	4	PG		EP1	EP2	EP3	RP	AD						ED1	ED2	ED3	PPG		BD
	5	PPG	BD	PG		EP1	EP2	EP3	RP	AD						ED1	ED2	ED3	PPG
	6	ED3	PPG		BD	PG		EP1	EP2	EP3	RP	AD						ED1	ED2
	7	ED1	ED2	ED3	PPG		BD	PG		EP1	EP2	EP3	RP	AD					
	8	AD		ED1	ED2	ED3	PPG		BD	PG		EP1	EP2	EP3	RP	AD			
	9	AD				ED1	ED2	ED3	PPG		BD	PG		EP1	EP2	EP3	RP	AD	

Legend: AD: adsorption, ED1: first equalisation depressurisation, ED2: second equalisation depressurisation, ED3: third equalisation depressurisation, PPG: providing purge, BD: blow down, PG: purge, EP1: first equalisation pressurisation, EP2: second equalisation pressurisation, EP3: third equalisation pressurisation, RP: repressurisation. $T_{AD} = t_{cycle}/3$, $t_{PPG} = t_{PG} = t_{cycle}/9$, $t_{BD} = t_{ED1} = t_{ED2} = t_{ED3} = t_{EP1} = t_{EP2} = t_{EP3} = t_{RP} = t_{cycle}/18$, $t_{cycle} = 300$ s.

Table 2
The layers' specification, dimensions and operating conditions.

Parameter	Value
Bed internal diameter, DB (m)	1.8
Bed Length (m)	AC: 8.5 m, Ze: 6.0 m
Feed flow rate (Nm3/h) (kmol/s)	(72,570) (0.9)
Feed pressure (bar)	25
Feed temperature (°C)	30
Feed composition (mol%)	79 % H2, 17 % CO_2, 2.1 % CH4, 1.2 % CO, 0.7 % N_2
Wall density, ρw (kg/m3)	783
Wall specific heat, Cpw (j/kg/K)	502.4
Particle density, ρp (kg/m3)	AC: 850, Ze: 1160
Particle specific heat, Cps(j/kg/K)	AC: 1047, Ze: 920
Particle porosity, ϵp (−)	AC: 0.61, Ze: 0.65
Bed porosity, ϵ (−)	AC: 0.433, Ze: 0.357
Particle diameter, dp (mm)	AC: 2.3, Ze: 3.14

The PSA process with all cycle steps outlined in Table 1 is modelled using Aspen Adsorption®, with mass, momentum, and energy balance partial differential equations (PDEs) listed in Table 3. The PDEs are converted to ordinary differential equations (ODEs) by discretising the bed height into 40 nodes through the Upwind Differencing Scheme 1 (UDS1). An implicit Euler integrator is used to solve the ODEs. The adsorption capacity of each gas on each adsorbent is calculated using Extended Langmuir 3, and kinetic behaviour is predicted by linear driving force (LDF) model with experimental mass transfer coefficients (MTCs), Table 4.

The H_2 purity (mol%) at the product (stream 2 of Fig. 1) is calculated after the CSS condition using Eq. (12), while the purity of gases at tail gas (stream 3 of Fig. 1) are calculated using Eqs. 13–17:

$$\text{Purity}\ (\%) = \frac{\int_O^{t_{ads}} C_{H2P} u_{sp} dt}{\sum_{i=1}^{n} \int_O^{t_{ads}} C_{ip} u_{sp} dt} \times 100 \quad 12$$

$$CO_2\ \text{Purity}\ (\%) = \frac{\left(\int_O^{t_{BD}} c_{CO_2 t} u_{st} + \int_O^{t_{PG}} c_{CO_2 t} u_{st}\right) dt}{\sum_{i=1}^{n} \left(\int_O^{t_{BD}} c_{it} u_{st} + \int_O^{t_{PG}} c_{it} u_{st}\right) dt} \times 100 \quad 13$$

$$CO\ \text{purity}\ (\%) = \frac{\left(\int_O^{t_{BD}} c_{COt} u_{st} + \int_O^{t_{PG}} c_{COt} u_{st}\right) dt}{\sum_{i=1}^{n} \left(\int_O^{t_{BD}} c_{it} u_{st} + \int_O^{t_{PG}} c_{it} u_{st}\right) dt} \times 100 \quad 14$$

$$N_2\ \text{Purity}\ (\%) = \frac{\left(\int_O^{t_{BD}} c_{N_2 t} u_{st} + \int_O^{t_{PG}} c_{N_2 t} u_{st}\right) dt}{\sum_{i=1}^{n} \left(\int_O^{t_{BD}} c_{it} u_{st} + \int_O^{t_{PG}} c_{it} u_{st}\right) dt} \times 100 \quad 15$$

Table 3
Formulas for mathematical modelling of cyclic adsorption units.

Description	Formulation	
gas phase mass balance for component i	$\frac{\partial}{\partial z}\left(\varepsilon D_z c_{gT} \frac{\partial y_i}{\partial z}\right) - \frac{\partial}{\partial z}(u_s c_{g,i}) - \varepsilon \frac{\partial c_{g,i}}{\partial t} - (1-\varepsilon)\rho_p \frac{\partial q_i}{\partial t} = 0$	(1)
Extended Langmuir 3 equation	$q_i^* = \frac{(k_{1,i} + k_{2,i} T) k_{3,i} e^{\frac{k_{4,i}}{T}} P_i}{1 + \sum_k k_{3,i} e^{\frac{k_{4,i}}{T}} P_i}$	(2)
Linear driving force (LDF) model for mass transfer	$\frac{\partial q_i}{\partial t} = MTC_i (q_i^* - q_i)$	(3)
The heat balance formula for bed wall	$\rho_w C_{pw} A_w \frac{\partial T_w}{\partial t} = 2\pi r_{bi} h_w (T_g - T_w) - 2\pi r_{bo} h_o (T_w - T_{atm})$	(4)
The heat balance formula for solid adsorbent	$(1-\varepsilon)\left[\rho_p \sum_{i=1}^{n} q_i C_{v,ads,i} + \rho_p C_{ps}\right] \frac{\partial T_p}{\partial t} = \rho_b \sum_{i=1}^{n} (-\Delta H_{ads})_i \frac{\partial q_i}{\partial t}$	(5)
The heat balance formula for the gas phase	$\frac{\partial}{\partial z}\left(\lambda \frac{\partial T_g}{\partial z}\right) - c_{gT} C_p \frac{\partial (u_s T_g)}{\partial z} - \varepsilon C_v T_g \frac{\partial c_{gT}}{\partial t} - (1-\varepsilon) a_p h_f (T_g - T_p) - \frac{4 h_w}{2 r_{bi}} (T_g - T_w) - \varepsilon c_{gT} C_v \frac{\partial T_g}{\partial t} = 0$	(6)
The formula for heat transfer from the gas phase to bed (Bird, 2002; Dantas et al., 2009, 2011; Reid et al., 1987)	$Nu_w = \frac{h_w 2 r_{bi}}{k_g} = 12.5 + 0.048\, Re$	(7)
The formula for effective axial heat dispersion coefficient (Wakao and Funazkri, 1978; R. T. Yang, 2013)	$\frac{\lambda}{k_g} = 7 + 0.5\, Re\, Pr$	(8)
The formula for heat transfer from bed wall to the atmosphere (Churchill and Chu, 1975; Vliet, 1969)	$Nu_o = \frac{h_o 2 r_{bo}}{k_a} = 0.1\, Ra^{1/3}$	(9)
The formula for heat transfer from solid adsorbent to gas phase (Wakao et al., 1979; Wakao and Funazkri, 1978)	$Nu_f = \frac{h_f d_p}{k_g} = 2 + 1.1\, Pr^{1/3} Re^{0.6}$	(10)
Pressure drop calculation by Ergun equation (Sereno and Rodrigues, 1993; J. Yang and Lee, 1998)	$-\frac{\partial P}{\partial z} = \frac{150\,\mu\,(1-\varepsilon)^2}{d_p^2\,\varepsilon^3} u_s + \frac{1.75\,(1-\varepsilon)\rho}{d_p\,\varepsilon^3} u_s \lvert u_s \rvert$	(11)

[a] Initial conditions (t = 0) are: $y_{CO_2} = y_{CH_4} = y_{N_2} = y_{CO} = 0; q_{CO_2} = q_{CH_4} = q_{N_2} = q_{CO} = 0; y_{H_2} = 1; T_g = T_p = T_w = T_{inlet}$

Table 4
Extended Langmuir isotherm and kinetic parameters for AC and Zeolite 5A adsorbents used for hydrogen purification case study (Ahn et al., 2012).

	K1 (mol/kg)	K2 (mol kg-1 K-1)	K3 (1/bar)	K4 (K)	ωi (1/s)
Activated Carbon					
CH_4	23.86	−0.0562	0.00348	1159	0.19
N_2	1.64	−0.00073	0.0545	326	0.26
CO	33.85	−0.0907	0.000231	1751	0.15
H_2	16.94	−0.021	0.0000625	1229	0.7
CO_2	28.79	−0.07	0.01	1030	0.035
Zeolite 5A					
CH_4	5.833	−0.01192	0.000605	1731	0.147
N_2	4.8133	−0.00668	0.000570	1531	0.099
CO	11.8454	−0.0313	0.0202	763	0.063
H_2	4.314	−0.0106	0.002515	458	0.7
CO_2	10.03	−0.01858	1.5781	207	0.0135

$$CH_4\ \text{Purity}\ (\%) = \frac{\left(\int_O^{t_{BD}} c_{CH_4 t} u_{st} + \int_O^{t_{PG}} c_{CH_4 t} u_{st}\right) dt}{\sum_{i=1}^{n}\left(\int_O^{t_{BD}} c_{it} u_{st} + \int_O^{t_{PG}} c_{it} u_{st}\right) dt} \times 100 \quad (16)$$

$$H_2\ \text{Purity}\ (\%) = \frac{\left(\int_O^{t_{BD}} c_{H_2 t} u_{st} + \int_O^{t_{PG}} c_{H_2 t} u_{st}\right) dt}{\sum_{i=1}^{n}\left(\int_O^{t_{BD}} c_{it} u_{st} + \int_O^{t_{PG}} c_{it} u_{st}\right) dt} \times 100 \quad (17)$$

where $c_{H_2 P}$ and c_{ip} are hydrogen and component i concentration at bed outlet while $c_{CO_2 t}$, $c_{H_2 t}$, c_{COt}, $c_{N_2 t}$ and $c_{CH_4 t}$ are CO_2, H_2, CO, N_2, and CH_4 concentration at tail gas, respectively. The terms u_{st} and u_{sp} are superficial velocity at tail and product gas, respectively. The hydrogen recovery is calculated using. Eq. (18):

$$\text{Recovery} = \frac{\int_O^{t_{ads}} C_{H2P} u_{sp} dt}{\int_O^{t_{feed}} C_{H2f} u_{sfeed} dt + \int_O^{t_{repress}} C_{H2f} u_{sfeed} dt} \quad (18)$$

2.2. Oxy-combustion process

The Aspen Plus® is used to simulate the oxy-combustion process, Fig. 2 with Peng-Robinson as equation of state. The tail gas (Stream TAILGAS2) enters an RGibbs reactor (OXYCOMBU), where combustion occurs in the presence of high-purity oxygen. The exhaust gas then enters the heat exchanger (COOLER1) to preheat the pure oxygen stream to a temperature where a temperature cross does not happen. Another exchanger (COOLER2) cools the gas to 200 °C that can be used for various applications in plant (e.g. steam production). A further cooling process is required for the exhaust gas before entering the condensation process (at 1 bar and 20 °C). Then, a portion of exhaust gas is recycled to the combustor, keeping the combustion temperature at the appropriate temperature (Khallaghi et al., 2019b). A cryogenic ASU is modelled with high- and low-pressure columns operated at 5.6 and 1.3 bar, respectively, and filled with 350Y structured packing (Khallaghi et al., 2021). The O_2 purity in the ASU is set at 95 % [18].

2.3. SOFC process

The SOFC is modelled using Aspen Plus®. The equations of state used for thermodynamic property estimation were the Peng-Robinson. The SOFC comprises a fuel preheater, anode and cathode cells, and afterburner, Fig. 3. The required oxygen for anode reactions was provided by air, while oxygen needed for complete combustion of unburned anode gases is supplied from semi-pure oxygen to avoid dilution of exhaust gas with N_2 present in the air. First, the tail gas (named "TAILGAS") is preheated with recycled exhaust gas (S6) from the afterburner in the fuel preheater (HEX1). Next, the heated tail gas enters the anode to react with oxygen supplied from the air in the cathode. The inlet air is preheated in one recuperator (HEX4) by the exhaust gas of the afterburner (streams S5). Finally, the heated air (stream S8) is conducted toward the cathode to supply the required oxygen for reactions in the anode.

To simulate the cathode, a separator (Sep) is used, and the separated oxygen flowrate (stream S9) toward the anode is calculated using Eq. (19) in a design-spec function of Aspen Plus® (Appleby, 1988; Campanari, 2001; Zhang et al., 2005):

$$n_{O_2 required} = 0.5 U_f n_{H_2 equivalent} \quad (19)$$

The term U_f is the fuel utilisation factor that is 85 %, and the term $n_{H_2 equivalent}$ represents the equivalent H_2 that can be produced from components in the tail gas that is calculated using Eq. (20) (Appleby, 1988; Campanari, 2001; Zhang et al., 2005):

$$n_{H_2 equivalent} = n_{H_2 in} + n_{COin} + 4 n_{CH_4 in} \quad (20)$$

The terms $n_{H_2 in}$, n_{COin} and $n_{CH_4 in}$ represent the hydrogen, CO, and CH_4 in the tail gas entering the fuel cell. The anode reactions were simulated by an equilibrium reactor (RGibbs) at a block named "ANODE", and effluent anode gas containing unburned H_2 and CO (stream S4) enters the afterburner for combustion with semi-pure oxygen (stream S17) that was pre-heated by depleted air of cathode from 30 to 758 °C in a preheater (HEX5). The Rstoic reactor was considered to simulate the afterburner using the below reactions for the complete conversion of CO and H_2:

$$CO + \frac{1}{2} O_2 \rightarrow CO_2 \quad (21)$$

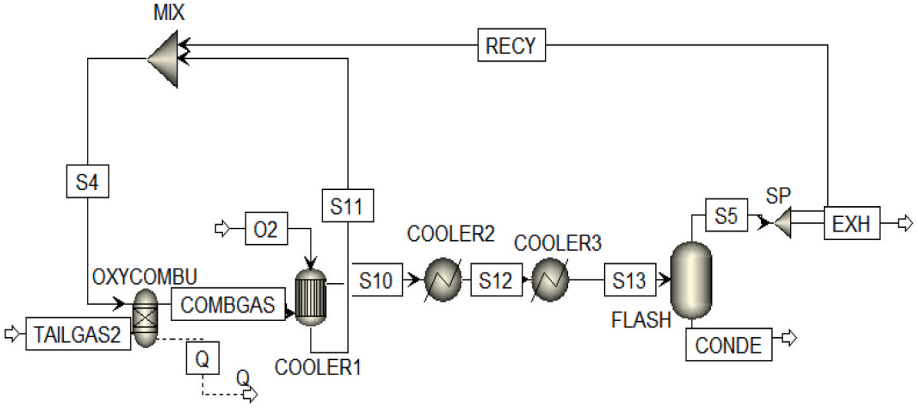

Fig. 2. Simulation flowsheet of oxy-combustion process in Aspen Plus®. Legend: MIX: mixer, SP: splitter, OXYCOMBU: furnace, solid lines: materials streams, and dotted lines: energy streams.

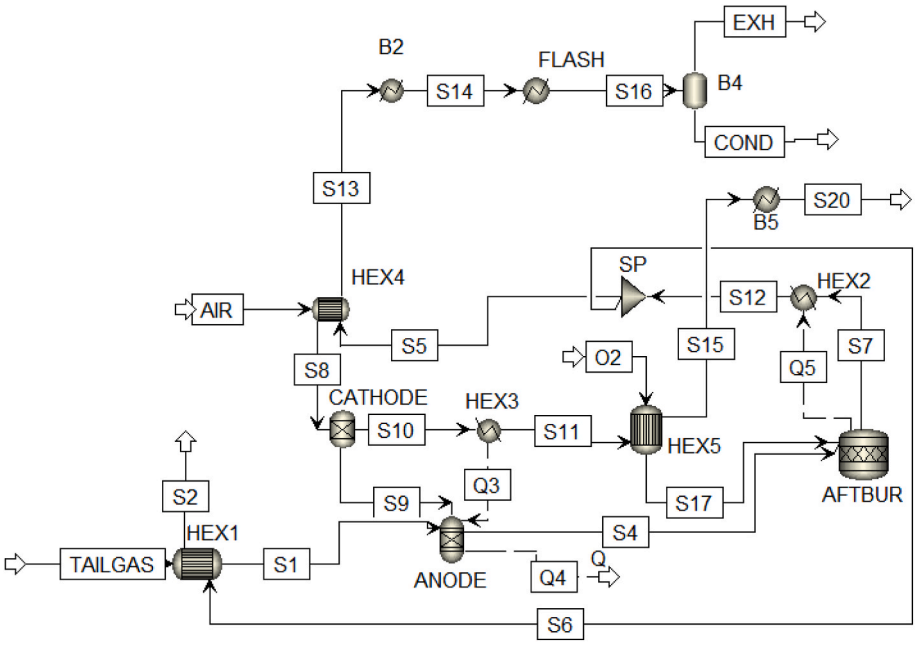

Fig. 3. Simulation flowsheet of SOFC in Aspen Plus®. Air is used as coolant and oxygen provider of the fuel cell, and semi-pure oxygen is used at afterburner—legend: solid lines: materials streams, and dotted lines: energy streams.

$$H_2 + \frac{1}{2}O_2 \rightarrow H_2O \tag{22}$$

The heat released in the afterburner is transferred to HEX2 to heat the combusted anode gas, and this gas pre-heats the inlet air in the recuperator (HEX4). The validation of the SOFC is presented in the supplementary material.

2.4. CLC process

The CLC process was modelled using built-in operation modules of Aspen Plus®. The simulation flowsheet depicts all the CLC elements, including the fuel reactor, air reactor, and separators, Fig. 4. The tail gas (Stream TAILGAS) enters an RGibbs equilibrium reactor (named "REDUCT") where reduction occurs (at 900 °C and 1 bar) with metal oxide (Cu2O). The effluent stream of the fuel reactor (stream H-EXH) (at 900 °C (Khallaghi et al., 2019a)) enters a separator (SEP1, SSplit) to separate the solids (mainly Cu and a little Cu_2O) and gases. The exchanger (COOLE1) recovers the heat of effluent gas (stream S3) and drops its temperature from 900 to 200 °C for various applications in the plant, such as steam production or preheating of process streams. The second exchanger (COOLE2) cools the exhaust gas to 20 °C to condense the moisture content in a flash drum (FLASH2). The solid stream (stream CU) enters another RGibbs equilibrium reactor (named "OXIDATIO"), where it is oxidised with hot air (stream H-AIR). The discharge stream of the air reactor (stream CU2OAIR) enters another separator (SEP2, SSplit) where solids (mainly Cu_2O and a little Cu) are separated from depleted air, then effluent solids (stream CU_2O) flow toward the fuel reactor.

3. Techno-economic assessment indicators

The thermodynamic performance of considered cases is evaluated based on the heat and work production/consumption (MW_{th} and MW_e) obtained from the simulation. On the other hand, the economic performance is assessed in terms of the levelised cost of hydrogen production (***LCOH***, €/***kg***), equation (23).

$$LCOH\left[\frac{€}{kg}\right] = \frac{TAC\left[\frac{M€}{y}\right]}{\dot{m}_{H2}\left[\frac{kg}{s}\right] \times 3600 \times 7884\left[\frac{h}{y}\right]} \times 1000 \tag{23}$$

The total annualised cost (TAC) has to be calculated by considering

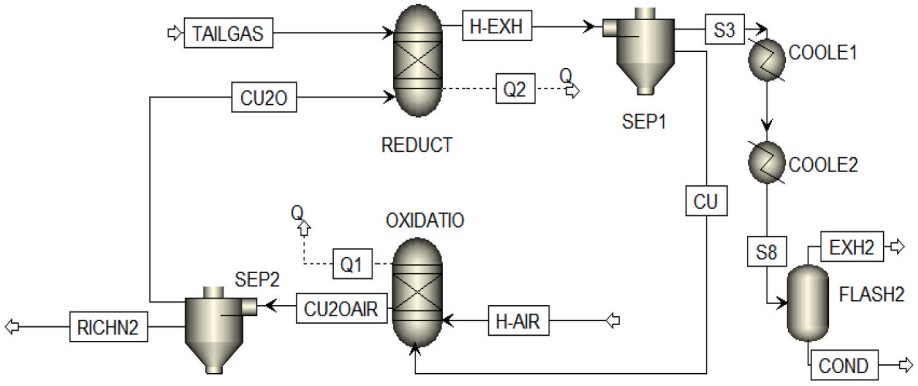

Fig. 4. Simulation flowsheet of CLC in Aspen Plus®. Legend: REDUCT: fuel reactor, SEP: separator, OXIDATIO: air reactor, solid lines: materials streams, and dotted lines: energy streams.

Table 5
Scaling parameters for the component purchase cost.

Component	Scaling factor	C_A (M€)	Q_A	Ref.
CLC plant	Fuel flowrate (t/h)	26	20	Cormos et al. (2020)
ASU unit	Oxygen flow rate (t/h)	143	220	Cormos et al. (2020)
Combustion chamber	Heat duty (MW)	0.81	19.78	Wallas (1990)
SOFC unit	Heat duty (MW)	11.5	6	Trendewicz and Braun (2013)
Heat exchanger	Heat transfer (MW)	6.1	828	Manzolini et al. (2020)

the total plant cost (TPC), the fuel cost (C_{fuel}), variable ($V_{O\&M}$), fixed ($F_{O\&M}$) operating and maintenance costs, using equation (24).

$$TAC\left[\frac{M€}{y}\right] = TPC \times ACCR + C_{fuel} + V_{O\&M} + F_{O\&M} \quad (24)$$

To calculate the ***TPC***, the equipment purchase costs ($\boldsymbol{C_B}$) is calculated based on reference cost data (Table 5) using equation (25) where $\boldsymbol{C_A}$ is the cost of the reference component with the capacity of $\boldsymbol{Q_A}$ and $\boldsymbol{f}$ is the scaling factor which is assumed to be 0.7 in this study.

$$C_B = C_A \left(\frac{Q_B}{Q_A}\right)^f \quad (25)$$

The total equipment cost (***TEC***) is calculated as in equation (26).

$$TEC = \sum_i^n C_{B,i} \quad (26)$$

TPC is calculated as in equation (27), which equals the sum of ***TEC***, total indirect cost (***TIC***), and the owner's cost ($\boldsymbol{C_{OC}}$). In which the ***TIC*** is assumed to be 30 % of ***TEC***, and the $\boldsymbol{C_{EPC}}$ is 15 % of the sum of ***TEC*** and ***TIC*** (Khallaghi et al., 2022).

$$TPC = TEC + TIC + C_{OC} \quad (27)$$

The annualised capital charge ratio (***ACCR***), is defined using equation (28), considering the project interest rate ($\boldsymbol{r}$) and project lifetime ($\boldsymbol{n}$).

$$ACCR = \frac{r(1+r)^n}{(1+r)^n - 1} \quad (28)$$

Assumptions for the calculation of the ***TAC*** are illustrated in Table 6.

Table 6
Assumptions for the economic analysis.

Parameter	Value	Ref.
Installation cost as a fraction of total purchase cost (%)	80	Khallaghi et al. (2022)
Variable operating cost (VOM) as a fraction of total capital cost (%)	2.0	Khallaghi et al. (2024)
Fixed operating cost (FOM) as a fraction of total capital cost (%)	1.0	Khallaghi et al. (2024)
Plant lifetime (T) (years)	30	Khallaghi et al. (2024)
Project interest rate (r) (%)	12	Khallaghi et al. (2024)
Fuel price (€/GJ)[a]	5	Khallaghi et al. (2024)
Capacity factor (CF) (%)	95	Khallaghi et al. (2024)

[a] The heat and electricity prices for the economic assessment are assumed to be 55 % and 400 % of the NG price, respectively.

4. Results and discussion

4.1. Performance of PSA and tail gas characterisation

The syngas of the SMR unit is modelled in the developed PSA model to calculate the hydrogen purity and recovery as well as the specifications of the tail gas, as shown in Supplementary Table 1. The PSA model has been validated in our previous studies (Golmakani et al., 2017, 2019, 2021). The model indicates that hydrogen purity after the PSA is 99.9 % at a recovery of 77.8 % with a total cycle time of 300 s. The pressure profile of this 9-bed PSA process shows that three equalisation steps have a considerable impact on pressure recovery in a manner that during the RP step, the bed is repressurised from 17.1 bar to 25 bar, Fig. 5a. The tail gas exits the bed during the BD and PG steps. It is observed that CO_2 purity increases during BD since CO_2 is desorbed at lower pressures, Fig. 5b. The tail gas flow rate is maximum at the beginning of the BD step and approaches zero due to the gradual reduction in bed pressure from 4.7 bar at the beginning to 1 bar at the end of the BD step, resulting in a drop in the driving force, Fig. 5c. To dampen the flow rate fluctuations of tail gas, a tail tank, Fig. 1, is provided downstream of PSA that stores the tail gas and injects it at a constant flow rate to downstream processes (SOFC, CLC, or oxy-combustion). The bed is repressurised with feed at 25 bar from 17.1 bar at the beginning of the RP step to 25 bar at its end; therefore, the RP flow rate gradually approaches zero in this step, Fig. 5d.

It is worth mentioning that the impurities in PSA tail gas mainly originate from the feed stream. These arise from (1) natural gas impurities like N_2, which persist through the SMR process (Golmakani et al., 2020); (2) unreacted CH_4, influenced by SMR efficiency, catalyst, and licensor (S. Wang et al., 2023); and (3) CO levels in the PSA feed, determined by shift reactor performance and catalyst choice (Chen and Chen, 2020). The PSA feed composition is based on typical composition from past studies, and Wang et al. have analysed the impact of these impurities on storage requirements (J. Wang et al., 2011).

4.2. Comparison of tail gas utilisation pathways

A sensitivity analysis of the oxy-combustion temperature was performed at three temperatures (1000, 1400, and 1700 °C); detailed results were provided in Supplementary Tables 2-4. The combustion temperature increment occurs with the heat recovery of the exhaust gas. It was shown that by increasing the temperature from 1000 to 1700 °C, the NO_x emission in the stack gas would increase from 4.8 to 290.1 ppm, Fig. 6a, since the higher flame temperatures favour the reaction of O_2 with N_2. The output heat from the combustion chamber decreases with the increase of flame temperature due to the more heat required for the rise of inlet gas temperature to flame temperature, Fig. 6b. The CO_2 purity at the stack gas decreases (from 92.7 % to 90.6 %) by increasing the flame temperature due to incomplete combustion of CO at high temperatures, Fig. 6c. The recovered heat rises with the increase in combustion chamber temperature due to the higher exit gas temperature, Fig. 6d. It can be concluded from this data that 1000 °C is the optimum temperature for the oxy-combustion process in terms of NO_x emission, CO_2 purity at the stack gas, and output heat.

The SOFC model was validated for a 100 kW atmospheric SOFC stack with natural gas as feedstock and operating conditions mentioned in Table 7.

The simulation flowsheet has an additional pre-reformer (REFOR) that converts heavy hydrocarbons and CH_4 to syngas, Fig. 7. The effluent anode gas (stream S5) is recycled to provide the required steam for the reforming reaction at a steam-to-carbon ratio 2.5. An ejector at the inlet provides a driving force for recycling anode gas. The experimental results and outputs of the SOFC model are provided in Table 8, and it is observed that the model can predict the experimental results with good precision. Supplementary Table 5 provides more details about the model.

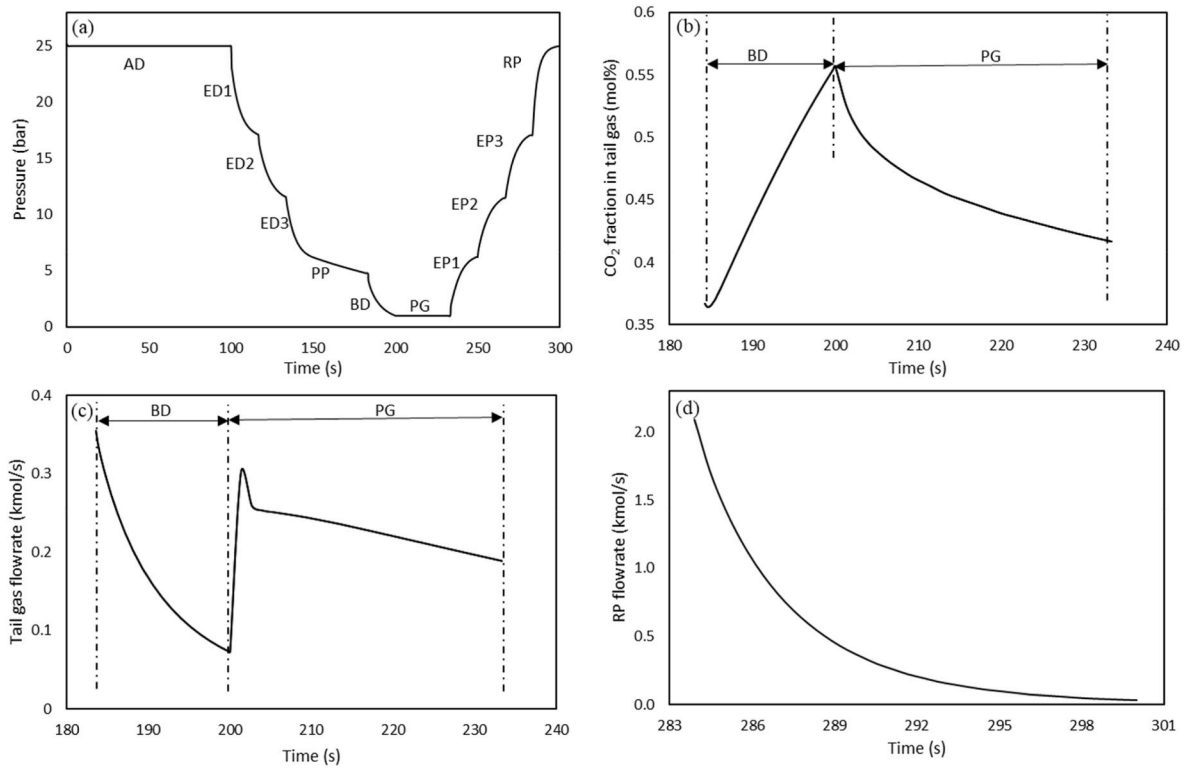

Fig. 5. The results after reaching cyclic steady-state conditions. (a) pressure profile, (b) CO_2 fraction in tail gas during BD and PG steps, (c) tail gas flowrate during BD and PG steps, (d) feed gas entering the bed during RP step.

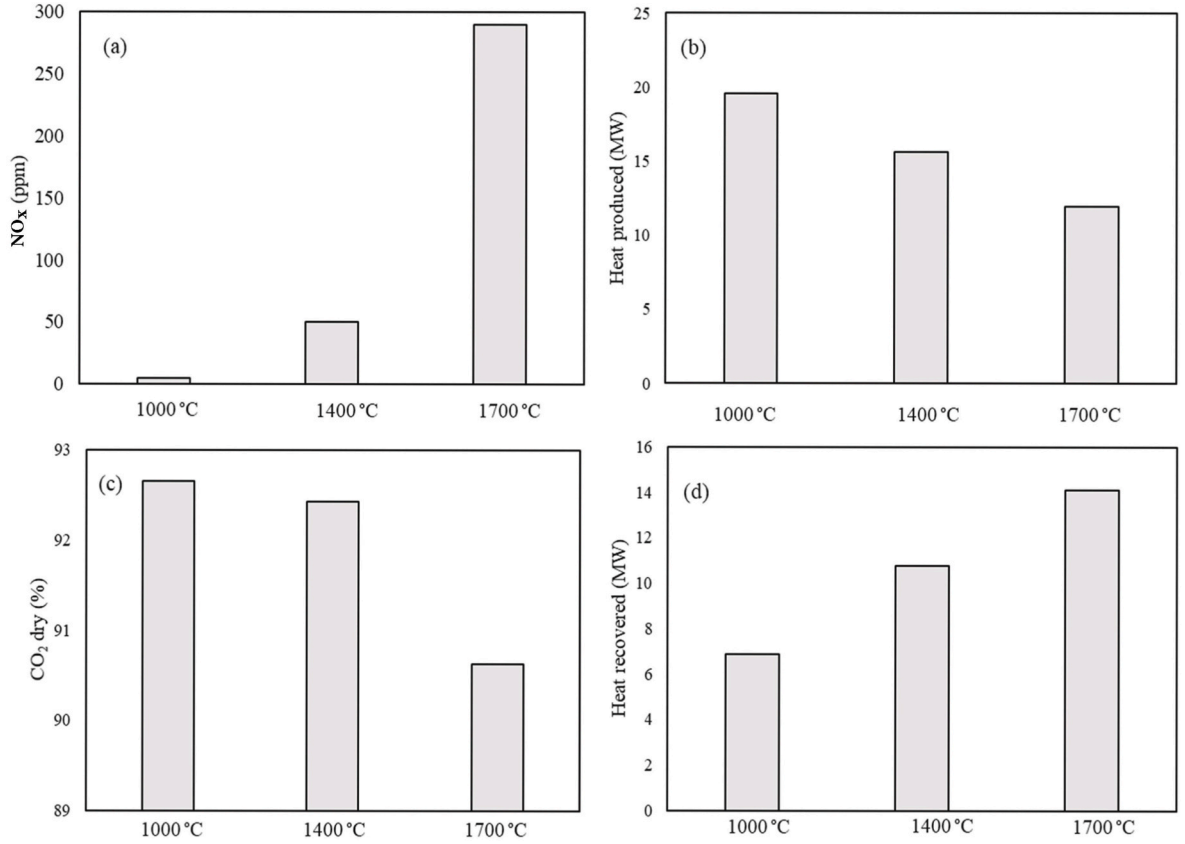

Fig. 6. The effect of temperature of the combustion chamber of the oxy-combustion process on (a) NOx emission, (b) heat output of furnace, (c) CO_2 purity in stack gas, and (d) recovered heat (MW).

Table 7
The operating conditions of the experimental SOFC test (Veyo, 1996; Veyo and Forbes, 1998; Veyo and Lundberg, 1999).

Parameters	Value
Fuel composition (mol%)	
CH_4	81.3
C_2H_6	2.9
C_3H_8	0.4
C_4H_{10}	0.2
N_2	14.3
CO	0.9
Turbomachinery	
SOFC temperature (°C)	910
SOFC pressure (bar)	1.08
SOFC power (kW)	120
Air temperature (°C)	630
Fuel temperature (°C)	200
afterburner efficiency (%)	100
steam to carbon ratio	2.5
Pressure drop (bar)	0

It is worth mentioning that, for SOFC integration, the reformer is deleted due to the high partial pressure of H_2 in the tail gas, which leads to the conversion of H_2 and CO to CH_4, which is not favourable. The recycle stream has also been deleted since there is no need to provide steam for the reforming reaction. The detailed results of the SOFC model are provided in Supplementary Table 6. The afterburner section of the SOFC model is the same as oxy-combustion. Still, the required oxygen demand is considerably lower (88 % lower) since most tail gas is oxidised with air for power generation at the anode. This shows that SOFC has more advantages than oxy-combustion due to the tail gas's simultaneous heat and power generation. The power efficiency of 52 % resulted in power generation of about 10.56 MW at the fuel cell output.

The most critical parameters for the CLC integration are oxygen carrier and airflow rates. The OC (Cu_2O) flow rate is adjusted to supply enough oxygen to reduce combustible gases in the tail gas to H_2O and CO_2. The overestimation of the OC flow rate (stream CU_2O) leads to the presence of Cu_2O with Cu, and underestimation leads to unburned H_2, CO, and CH_4 at the outlet of the fuel reactor (stream H-EXH). The airflow rate (stream H-AIR) is optimised in a manner that all Cu (stream CU) is oxidised to copper oxide (Cu_2O). The underestimation of airflow rate leads to Cu with Cu_2O, and overestimation leads to a high amount of O_2 at the outlet of the air reactor (stream RICHN2). Therefore, the airflow should be adjusted so that the oxygen carrier (Cu) can be oxidised entirely (Cu_2O). The heat production from air and fuel reactors is 14.45 MW, while the recovered heat is 5.93 MW (heat recovered by COOLE1).

Another parameter that needs attention is the CO_2 purity in the stack gas, Fig. 8. CLC with higher CO_2 purity (95 %) than other cases is more attractive as no further CO_2 purification is needed than SOFC and oxy-combustion cases, which have CO_2 purities of 94.1 % and 92.6 %, respectively.

4.3. Techno-economic performance

Table 9 presents a comparative assessment of three hydrogen production system configurations. These results highlight the trade-offs between different configurations, particularly regarding capital investment, operational costs, and energy efficiency, offering insights into the

Table 8
Comparison of the SOFC model and experimental results.

Parameters	Experimental data (Veyo, 1996; Veyo and Forbes, 1998; Veyo and Lundberg, 1999)	Model output
Reformer outlet temperature (°C)	550	537
Effluent stream of anode composition (stream S4) (mol%)	48 % H_2O, 28 % CO_2, 14 % H_2, 5 % CO, 5 % N_2	50.9 % H_2O, 24.9 % CO_2, 11.6 % H_2, 7.4 % CO, 5.1 % N_2
Stack gas composition (stream S13) (mol%)	77 % N_2, 16 %O_2, 5 % H_2O, 2 % CO_2	77.3 % N_2, 15.9 % O_2, 4.5 % H_2O, 2.3 %CO_2
Stack gas temperature (°C)	847	834

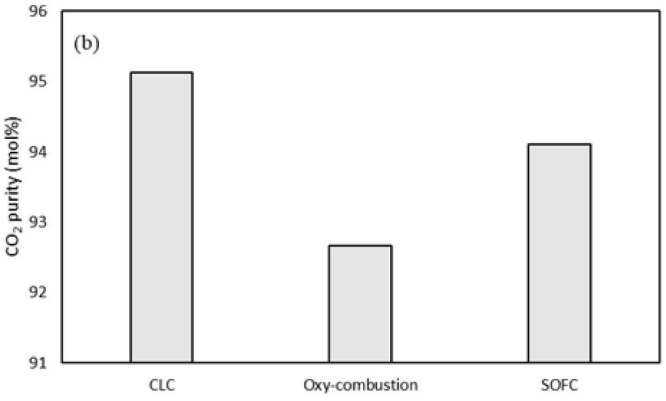

Fig. 8. CO_2 purity comparison of SOFC, oxy-combustion, and CLC.

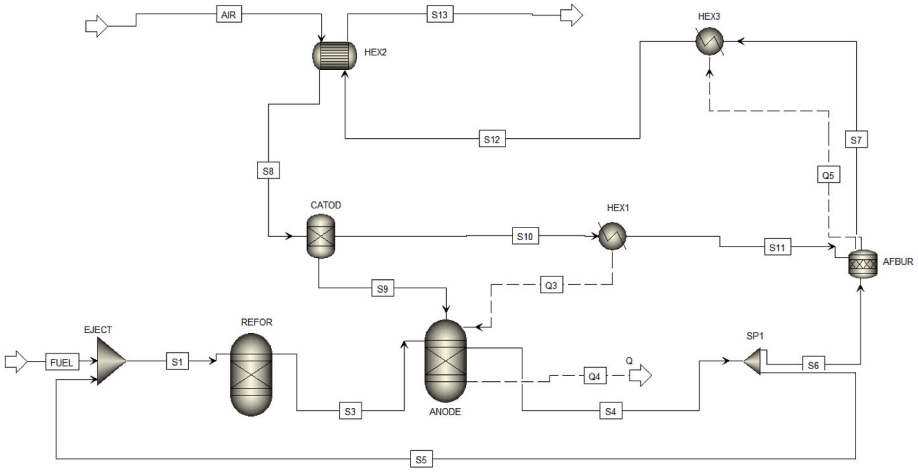

Fig. 7. Simulation flowsheet of SOFC in Aspen Plus® for the case that air is used as a coolant and oxygen provider. Legend: solid lines: materials streams, and dotted lines: energy streams. Circles: temperature.

Table 9
Economic performance of hydrogen production with tail gas capturing using SOFC, oxy-combustion, and CLC processes.

	Unit	SOFC	Oxy-comb.	CLC
Technical comparison				
Heat production	[MW_{th}]	10.6	26.5	20.4
Power production	[MW_e]	10.6	–	–
Power consumption (ASU)	[MW_e]	0.2[a]	1.5[a]	–
Economic comparison				
H_2 production plant (Al Lagtah et al., 2019)	[M€]	204.2	204.2	204.2
CLC plant	[M€]	–	–	20.0
ASU	[M€]	3.6	13.4	–
Combustion chamber	[M€]	–	0.8	–
SOFC unit	[M€]	21.8	–	–
Total equipment cost (TEC)	[M€]	229.6	218.3	224.2
Indirect capital costs (TIC)	[M€]	68.9	65.5	67.3
Owner's costs (OC)	[M€]	44.8	42.6	43.7
Total plant cost (TPC)	[M€]	343.2	326.6	335.2
Annualised plant cost	[M€/y]	42.5	40.4	41.5
Variable operation and maintenance ($V_{O\&M}$)	[M€/y]	3.4	3.2	3.3
Fixed operation and maintenance ($F_{O\&M}$)	[M€/y]	6.9	3.26.5	6.7
Electricity revenue	[M€/y]	2.9	–	–
Electricity cost	[M€/y]	–	0.4	–
Heat revenue	[M€/y]	0.9	2.2	2.7
Fuel Cost	[M€/y]	43.7	43.7	43.7
Total annualised cost	[M€/y]	92.7	92.1	93.9
LCOH	[€/kg]	1.9	1.9	1.9

[a] The power requirement for ASU is assumed to be 0.75 MJ/kg_{O2} (Khallaghi et al., 2021).

economic feasibility of integrating SOFC, oxy-combustion, or CLC into hydrogen production. In terms of thermal energy output, the oxy-combustion system produces the highest heat production (26.5 MW_{th}), followed by the CLC system (20.4 MW_{th}) and the SOFC system (10.6 MW_{th}). The SOFC system is the only configuration generating electrical power (10.6 MW_{el}), while oxy-combustion and CLC systems rely on external power sources. The air separation unit (ASU) required for oxy-combustion has the highest power consumption (1.5 MW_{el}). In comparison, SOFC has a marginal ASU-related power demand (0.2 MW_{el}), and CLC does not require an ASU. From an economic perspective, the base hydrogen production plant cost is identical across all configurations (204.2 M€). However, additional capital costs vary depending on system components. The SOFC unit adds 21.8 M€ to the total equipment cost (TEC), whereas the oxy-combustion system requires an ASU (13.4 M€) and a combustion chamber (0.8 M€). The CLC system incurs a dedicated reactor cost of 20.0 M€, but does not require an ASU. Consequently, the total plant cost is lowest for the oxy-combustion system (326.6 M€), followed by CLC (335.2 M€) and SOFC (343.2 M€). Annualised costs show minor variations between configurations, ranging from 92.1 M€/y for oxy-combustion to 93.9 M€/y for CLC. The SOFC system benefits from electricity revenue (2.9 M€/y), whereas oxy-combustion incurs an electricity cost of 0.4 M€/y. Heat revenues differ, with CLC achieving the highest revenue (2.7 M€/y), followed by oxy-combustion (2.2 M€/y) and SOFC (0.9 M€/y). Despite these differences, the levelised cost of hydrogen remains constant at 1.9 €/kg across all systems.

A sensitivity analysis was conducted on fuel cost, interest rate, and CAPEX, Fig. 9. The results indicate that a ±30 % variation in fuel price and interest rate leads to a ±13 % change in the LCOH for the SOFC case, ranging from 1.7 to 2.2 €/kg_{H2}. Similarly, a ±30 % change in CAPEX causes the LCOH to vary between 1.6 and 2.3 €/kg_{H2}. A comparable trend is observed for oxy-combustion and CLC. In these cases, a ±30 % change in fuel price and interest rate results in a 13 % variation in LCOH, ranging from 1.66 to 2.18 €/kg_{H2} for oxy-combustion and 1.69 to 2.2 €/kg_{H2} for CLC. Meanwhile, the same CAPEX variations lead to a 16 % change in LCOH, with values ranging from 1.6 to 2.24 €/kg_{H2} for oxy-combustion and 1.6 to 2.3 €/kg_{H2} for CLC.

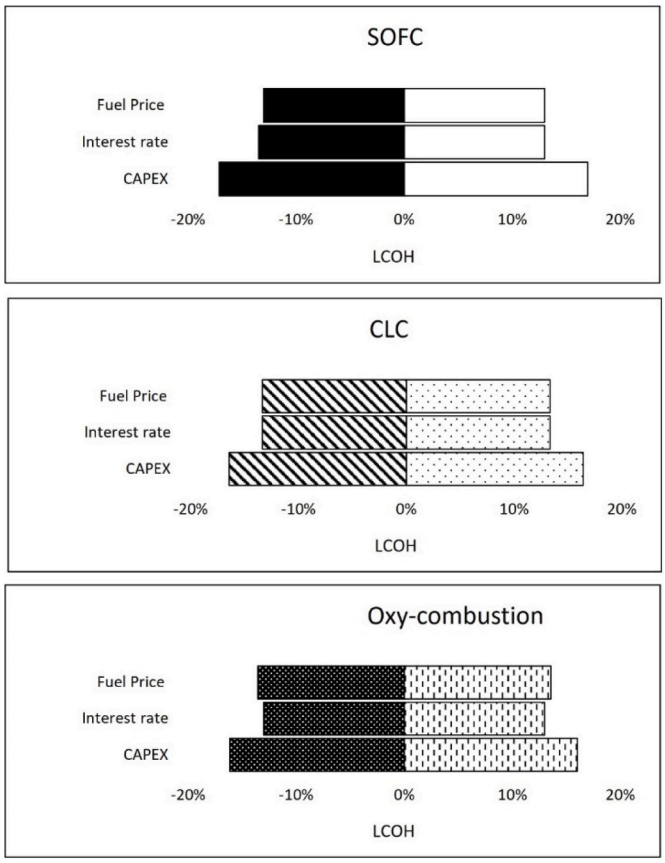

Fig. 9. Sensitivity analysis of Fuel price, interest rate and CAPEX.

4.4. Implications for industrial integration and future outlook

Although all three cases show similar economic performance with the hydrogen production cost of 1.9 €/kg_{H2}, each case can be of interest for specific industrial purposes. For example, available heat for each case can supplement and compensate for the existing heat requirement of an industrial site or district heating. However, the power generation in SOFC can also help reduce the energy required for other auxiliaries' power consumption. The techno-economic assessment conducted in this study reveals that hydrogen production using all three options offers competitive cost performance compared to the current state-of-the-art technology. Specifically, SMR without CCS achieves an LCOH of approximately 1 €/$kg_{H2,}$ while integrating CCS increases the LCOH to around 1.5 €/kg_{H2} (NETL, 2022). In comparison, coal gasification coupled with CCS results in a significantly higher LCOH of 2.8 €/kg_{H2} (NETL, 2022), largely due to the additional expenses involved in capturing and storing CO_2 from coal-based processes. On the other hand, electrolysis using grid electricity remains a costly option, with an LCOH ranging between 3.0 and 6 €/kgH_2. However, when electrolysis is powered by renewable energy sources such as solar or wind, the cost of hydrogen production can become more competitive, with an LCOH ranging from 1.7 to 3.7 €/kgH_2, depending on factors like electricity prices and electrolyser efficiency (IEA, 2019). These results demonstrate the potential for the proposed technologies to reduce the cost of hydrogen production, particularly when integrated with carbon capture or renewable energy solutions, positioning them as viable alternatives for achieving low-cost, low-carbon hydrogen production.

However, hybrid approaches, such as integrating CLC with membrane separation or SOFCs, can be explored to optimise hydrogen

recovery and energy efficiency. A comprehensive life cycle assessment is necessary to evaluate the environmental impact and sustainability of these decarbonisation strategies compared to conventional CO_2 capture methods. Moreover, integrating the proposed technologies with renewable hydrogen production pathways, such as biomass gasification or electrolysis, could enhance system flexibility and reduce reliance on fossil-based hydrogen.

5. Conclusion

The dilemma of reducing greenhouse gas emissions triggered the roll-out of hydrogen production technologies, with SMR as the most promising technology until the TRL of greener technologies is improved to commercial levels. However, SMR technology emits a considerable amount of CO_2 via PSA tail gas, which is currently burned at the reformer of this unit, resulting in a low CO_2 purity stack gas that is costly to capture. The amine, adsorption, and membrane technologies have already been investigated to capture CO_2 from PSA tail gas. However, we aim to investigate SOFC, CLC, and oxy-combustion that can operate at atmospheric conditions; therefore, there is no additional cost for the compressor to increase the tail gas pressure. Firstly, to find the optimum alternative, a PSA process at an industrial scale was modelled to calculate the tail gas composition and flow rate. Then, this gas is treated via three options, including SOFC, CLC, and oxy-combustion. Although the techno-economic analysis revealed that all three options are competitive with a hydrogen production cost of 1.9 €/kg_{H2}, it was shown that the CO_2 purity of CLC is adequate to capture (>95 %) without any further CO_2 purification implementation.

CRediT authorship contribution statement

Ayub Golmakani: Writing – original draft, Software, Methodology, Formal analysis, Data curation, Conceptualization. **Navid Khallaghi:** Writing – review & editing, Validation, Data curation. **Amirpiran Amiri:** Validation, Software, Data curation. **Vasilije Manovic:** Writing – review & editing, Supervision. **Seyed Ali Nabavi:** Writing – review & editing, Supervision, Project administration.

Declaration of competing interest

The authors declare that they have no known competing financial interests or personal relationships that could have appeared to influence the work reported in this paper.

Appendix A. Supplementary data

Supplementary data to this article can be found online at https://doi.org/10.1016/j.jgsce.2025.205683.

Data availability

No data was used for the research described in the article.

References

Ahn, S., You, Y.-W., Lee, D.-G., Kim, K.-H., Oh, M., Lee, C.-H., 2012. Layered two-and four-bed PSA processes for H2 recovery from coal gas. Chem. Eng. Sci. 68 (1), 413–423.

Al Lagtah, N.M.A., Onaizi, S.A., Albadarin, A.B., Ghaith, F.A., Nour, M.I., 2019. Techno-economic analysis of the effects of heat integration and different carbon capture technologies on the performance of coal-based IGCC power plants. J. Environ. Chem. Eng. 7 (6), 103471. https://doi.org/10.1016/j.jece.2019.103471.

Appleby, A.J., 1988. Fuel Cell Handbook.

Barbarias, I., Lopez, G., Artetxe, M., Arregi, A., Bilbao, J., Olazar, M., 2018. Valorisation of different waste plastics by pyrolysis and in-line catalytic steam reforming for hydrogen production. Energy Convers. Manag. 156, 575–584.

Bird, R.B., 2002. Transport phenomena. Appl. Mech. Rev. 55 (1), R1–R4.

Campanari, S., 2001. Thermodynamic model and parametric analysis of a tubular SOFC module. J. Power Sources 92 (1–2), 26–34.

Chen, W.H., Chen, C.Y., 2020. Water gas shift reaction for hydrogen production and carbon dioxide capture: a review. In: Applied Energy, vol. 258. Elsevier Ltd. https://doi.org/10.1016/j.apenergy.2019.114078.

Cho, S.-H., Chue, K.-T., Kim, J.-N., 1998. A two stage PSA for argon and hydrogen recovery from ammonia purge gas. Chem. Eng. Commun. 163 (1), 97–109.

Churchill, S.W., Chu, H.H.S., 1975. Correlating equations for laminar and turbulent free convection from a horizontal cylinder. Int. J. Heat Mass Tran. 18 (9), 1049–1053.

Cormos, A.-M., Dumbrava, I., Cormos, C.-C., 2020. Evaluation of techno-economic performance for decarbonized hydrogen and power generation based on glycerol thermo-chemical looping cycles. Appl. Therm. Eng. 179, 115728. https://doi.org/10.1016/j.applthermaleng.2020.115728.

Dantas, T.L.P., Amorim, S.M., Luna, F.M.T., Silva, I.J., de Azevedo, D.C.S., Rodrigues, A. E., Moreira, R.F.P.M., 2009. Adsorption of carbon dioxide onto activated carbon and nitrogen-enriched activated carbon: surface changes, equilibrium, and modeling of fixed-bed adsorption. Separ. Sci. Technol. 45 (1), 73–84. https://doi.org/10.1080/01496390903401762.

Dantas, T.L.P., Luna, F.M.T., Silva Jr., I.J., de Azevedo, D.C.S., Grande, C.A., Rodrigues, A.E., Moreira, R.F.P.M., 2011. Carbon dioxide–nitrogen separation through adsorption on activated carbon in a fixed bed. Chem. Eng. J. (Amsterdam, Neth.) 169 (1–3), 11–19.

Duman, G., Yanik, J., 2017. Two-step steam pyrolysis of biomass for hydrogen production. Int. J. Hydrogen Energy 42 (27), 17000–17008.

Golmakani, A., Ali Nabavi, S., Wadi, B., Manovic, V., 2022. Advances, challenges, and perspectives of biogas cleaning, upgrading, and utilisation. Fuel (Guildf.) 317, 123085. https://doi.org/10.1016/j.fuel.2021.123085.

Golmakani, A., Fatemi, S., Tamnanloo, J., 2016. CO2 capture from the tail gas of hydrogen purification unit by vacuum swing adsorption process, using SAPO-34. Ind. Eng. Chem. Res. 55 (1), 334–350. https://doi.org/10.1021/acs.iecr.5b02690.

Golmakani, A., Fatemi, S., Tamnanloo, J., 2017. Investigating PSA, VSA, and TSA methods in SMR unit of refineries for hydrogen production with fuel cell specification. Separ. Purif. Technol. 176, 73–91. https://doi.org/10.1016/j.seppur.2016.11.030.

Golmakani, A., Nabavi, S.A., Manović, V., 2019. Effect of impurities on ultra-pure hydrogen production by pressure vacuum swing adsorption. J. Ind. Eng. Chem. 82, 278–289.

Golmakani, A., Nabavi, S.A., Manović, V., 2020. Effect of impurities on ultra-pure hydrogen production by pressure vacuum swing adsorption. J. Ind. Eng. Chem. 82, 278–289. https://doi.org/10.1016/j.jiec.2019.10.024.

Golmakani, A., Nabavi, S.A., Manović, V., 2021. Production of negative-emission biomethane by twin double-bed pressure swing adsorption with tail gas sequestration. Chem. Eng. J. (Amsterdam, Neth.) 408, 127312.

Higman, C., 2008. Gasification. In: Combustion Engineering Issues for Solid Fuel Systems. Elsevier, pp. 423–468.

IEA, 2019. The Future of Hydrogen.

Khallaghi, N., Abbas, S.Z., Manzolini, G., De Coninck, E., Spallina, V., 2022. Techno-economic assessment of blast furnace gas pre-combustion decarbonisation integrated with the power generation. Energy Convers. Manag. 255 (January), 115252. https://doi.org/10.1016/j.enconman.2022.115252.

Khallaghi, N., Ghiami, S., Jeswani, H., Nabavi, S.A., Anthony, E.J., 2024. Blue hydrogen production through partial oxidation: a techno-economic and life cycle assessment. Int. J. Energy Res. 2024 (1). https://doi.org/10.1155/er/3249514.

Khallaghi, N., Hanak, D.P., Manovic, V., 2019a. Gas-fired chemical looping combustion with supercritical CO2 cycle. Appl. Energy 249, 237–244. https://doi.org/10.1016/j.apenergy.2019.04.096.

Khallaghi, N., Hanak, D.P., Manovic, V., 2019b. Staged oxy-fuel natural gas combined cycle. Appl. Therm. Eng. 153. https://doi.org/10.1016/j.applthermaleng.2019.03.033.

Khallaghi, N., Hanak, D.P., Manovic, V., 2020. Techno-economic evaluation of near-zero CO2 emission gas-fired power generation technologies : a review. J. Nat. Gas Sci. Eng. 74, 103095. https://doi.org/10.1016/j.jngse.2019.103095.

Khallaghi, N., Jeswani, H., Hanak, D.P., Manovic, V., 2021. Techno-economic-environmental assessment of biomass oxy-gasification staged oxy-combustion for negative emission combined heat and power. Appl. Therm. Eng. 196 (November 2020), 117254. https://doi.org/10.1016/j.applthermaleng.2021.117254.

Li, B., He, G., Jiang, X., Dai, Y., Ruan, X., 2016. Pressure swing adsorption/membrane hybrid processes for hydrogen purification with a high recovery. Front. Chem. Sci. Eng. 10 (2), 255–264. https://doi.org/10.1007/s11705-016-1567-1.

Manzolini, G., Giuffrida, A., Cobden, P.D., van Dijk, H.A.J., Ruggeri, F., Consonni, F., 2020. Techno-economic assessment of SEWGS technology when applied to integrated steel-plant for CO2 emission mitigation. Int. J. Greenh. Gas Control 94 (February 2019), 102935. https://doi.org/10.1016/j.ijggc.2019.102935.

Mehrpooya, M., Habibi, R., 2020. A review on hydrogen production thermochemical water-splitting cycles. J. Clean. Prod., 123836

NETL, 2022. COMPARISON OF COMMERCIAL, STATE-OF-THE-ART, FOSSIL-BASED HYDROGEN PRODUCTION TECHNOLOGIES.

Pellegrini, L.A., De Guido, G., Moioli, S., 2020. Design of the CO2 removal section for PSA tail gas treatment in a hydrogen production plant. Front. Energy Res. 8, 77.

Pinsky, R., Sabharwall, P., Hartvigsen, J., O'Brien, J., 2020. Comparative review of hydrogen production technologies for nuclear hybrid energy systems. Prog. Nucl. Energy 123, 103317.

Reed, C.L., Kuhre, C.J., 1980. Hydrogen Production from Partial Oxidation of Residual Fuel Oil. ACS Publications.

Reid, R.C., Prausnitz, J.M., Poling, B.E., 1987. The Properties of Gases and Liquids.

Schneider, S., Bajohr, S., Graf, F., Kolb, T., 2020. State of the art of hydrogen production via pyrolysis of natural gas. ChemBioEng Rev. 7 (5), 150–158.

Sereno, C., Rodrigues, A., 1993. Can steady-state momentum equations be used in modelling pressurization of adsorption beds? Gas Separ. Purif. 7 (3), 167–174. https://doi.org/10.1016/0950-4214(93)80006-I.

Seyitoglu, S.S., Dincer, I., Kilicarslan, A., 2017. Energy and exergy analyses of hydrogen production by coal gasification. Int. J. Hydrogen Energy 42 (4), 2592–2600. https://doi.org/10.1016/j.ijhydene.2016.08.228.

Steinberg, M., Cheng, H.C., 1989. Modern and prospective technologies for hydrogen production from fossil fuels. Int. J. Hydrogen Energy 14 (11), 797–820. https://doi.org/10.1016/0360-3199(89)90018-9.

Tamnanloo, J., Fatemi, S., & Golmakani, A. (n.d.). Binary Equilibrium Adsorption Data and Comparison of Zeolites with Activated Carbon for Selective Adsorption of CO 2 from CH 4.

Trendewicz, A.A., Braun, R.J., 2013. Techno-economic analysis of solid oxide fuel cell-based combined heat and power systems for biogas utilization at wastewater treatment facilities. J. Power Sources 233, 380–393. https://doi.org/10.1016/j.jpowsour.2013.01.017.

Veyo, S.E., 1996. The Westinghouse solid oxide fuel cell program-a status report. In: IECEC 96. Proceedings of the 31st Intersociety Energy Conversion Engineering Conference, vol.2, pp. 1138–1143.

Veyo, S.E., Forbes, C., 1998. Demonstrations based on Westinghouse's prototype commercial AES design. Third Eur. Solid Oxide Fuel Cell Forum. Proc. Oral Present. 79–86.

Veyo, S.E., Lundberg, W.L., 1999. Solid oxide fuel cell power system cycles. Turbo Expo: Power for Land, Sea, and Air 78590, V002T02A058.

Vliet, G.C., 1969. Natural Convection Local Heat Transfer on Constant-Heat-Flux Inclined Surfaces.

Wakao, N., Funazkri, T., 1978. Effect of fluid dispersion coefficients on particle-to-fluid mass transfer coefficients in packed beds: correlation of sherwood numbers. Chem. Eng. Sci. 33 (10), 1375–1384. https://doi.org/10.1016/0009-2509(78)85120-3.

Wakao, N., Kaguei, S., Funazkri, T., 1979. Effect of fluid dispersion coefficients on particle-to-fluid heat transfer coefficients in packed beds: correlation of nusselt numbers. Chem. Eng. Sci. 34 (3), 325–336. https://doi.org/10.1016/0009-2509(79)85064-2.

Wallas, S.M., 1990. Chemical process equipment. In: Selection and Design. Butterworth-Heinemann, Elsevier, Oxford UK.

Wang, J., Ryan, D., Anthony, E.J., Wildgust, N., Aiken, T., 2011. Effects of impurities on CO2 transport, injection and storage. Energy Proc. 4, 3071–3078. https://doi.org/10.1016/j.egypro.2011.02.219.

Wang, S., Nabavi, S.A., Clough, P.T., 2023. A review on bi/polymetallic catalysts for steam methane reforming. In: International Journal of Hydrogen Energy, vol. 48. Elsevier Ltd, pp. 15879–15893. https://doi.org/10.1016/j.ijhydene.2023.01.034. Issue 42.

Yáñez, M., Relvas, F., Ortiz, A., Gorri, D., Mendes, A., Ortiz, I., 2020. PSA purification of waste hydrogen from ammonia plants to fuel cell grade. Separ. Purif. Technol. 240, 116334. https://doi.org/10.1016/j.seppur.2019.116334.

Yang, J., Lee, C., 1998. Adsorption dynamics of a layered bed PSA for H2 recovery from coke oven gas. AIChE J. 44 (6), 1325–1334.

Yang, R.T., 2013. Gas Separation by Adsorption Processes. Butterworth-Heinemann.

Zhang, W., Croiset, E., Douglas, P.L., Fowler, M.W., Entchev, E., 2005. Simulation of a tubular solid oxide fuel cell stack using AspenPlusTM unit operation models. Energy Convers. Manag. 46 (2), 181–196. https://doi.org/10.1016/j.enconman.2004.03.002.

Zhou, Q., Zhong, X., Xie, X., Jia, X., Chen, B., Wang, N., Huang, L., 2020. Auto-thermal reforming of acetic acid for hydrogen production by ordered mesoporous Ni-xSm-Al-O catalysts: effect of samarium promotion. Renew. Energy 145, 2316–2326.